The role of the Met^{20} loop in the hydride transfer in *Escherichia coli* dihydrofolate reductase

Received for publication, January 17, 2017, and in revised form, May 24, 2017 Published, Papers in Press, June 15, 2017, DOI 10.1074/jbc.M117.777136

Anil R. Mhashal[‡1], **Alexandra Vardi-Kilshtain**[‡1], **Amnon Kohen**[§], **and Dan Thomas Major**[‡2]

From the [‡]*Department of Chemistry and the Lise Meitner-Minerva Center of Computational Quantum Chemistry, Bar-Ilan University, Ramat-Gan 5290002, Israel and* [§]*Department of Chemistry, University of Iowa, Iowa City, Iowa 52242*

Edited by Ruma Banerjee

A key question concerning the catalytic cycle of *Escherichia coli* dihydrofolate reductase (*ec*DHFR) is whether the Met^{20} loop is dynamically coupled to the chemical step during catalysis. A more basic, yet unanswered question is whether the Met^{20} loop adopts a closed conformation during the chemical hydride transfer step. To examine the most likely conformation of the Met^{20} loop during the chemical step, we studied the hydride transfer in wild type (WT) *ec*DHFR using hybrid quantum mechanics-molecular mechanics free energy simulations with the Met^{20} loop in a closed and disordered conformation. Additionally, we investigated three mutant forms (I14*X*; *X* = Val, Ala, Gly) of the enzyme that have increased active site flexibility and donor-acceptor distance dynamics in closed and disordered Met^{20} loop states. We found that the conformation of the Met^{20} loop has a dramatic effect on the ordering of active site hydration, although the Met^{20} loop conformation only has a moderate effect on the hydride transfer rate and donor-acceptor distance dynamics. Finally, we evaluated the pK_a of the substrate N5 position in closed and disordered Met^{20} loop states and found a strong correlation between N5 basicity and the conformation of the Met^{20} loop.

Escherichia coli dihydrofolate reductase (*ec*DHFR)[3] serves as a benchmark enzyme for the study of static and dynamic effects in biocatalysis (1). DHFR catalyzes the reduction of dihydrofolate (DHF or H_2folate) by nicotinamide adenine dinucleotide phosphate hydride (NADPH) to form tetrahydrofolate (H_4folate) and $NADP^+$ (Scheme 1). Its principal function is to maintain intracellular pools of H_4folate, a compound essential for the biosynthesis of purines, thymine nucleotides, and several amino acids.

The Met^{20} loop in *ec*DHFR is a flexible structural motif that closes and opens the active site cleft as ligands bind or dissociate from the enzyme. The Met^{20} loop dynamics have been suggested to occur on the pico- to millisecond timescale (2), and an important question is whether any of its motions are coupled to catalysis (3–5). It has been proposed that the Met^{20} loop (residues 9–23) may adopt three principle states, open, closed, and occluded (6), and the conformation of the Met^{20} loop has been proposed to correlate with catalysis (6–11). For instance, Brooks and co-workers (12–14) suggested that rapid hydride transfer is correlated with a selected subset of Met^{20} conformational states. This raises the question of whether the Met^{20} loop is closed during the chemical step and more generally whether the Met^{20} loop plays a role during hydride transfer.

To investigate this question, we studied the hydride transfer in wild type (WT) *ec*DHFR and three Met^{20} loop mutant enzymes, namely I14V, I14A, and I14G. These mutants have been shown to possess increased active site flexibility relative to the WT enzyme and, in particular, enhanced donor-acceptor distance (DAD) dynamics (15, 16). This DAD dynamics perturbation has a rather radical effect on the temperature dependence of the kinetic isotope effect (KIE) (15, 17). In the WT enzyme, the KIE is temperature-independent, whereas the KIE becomes increasingly temperature-dependent as the steric effect of the mutation becomes more pronounced. In the crystal structures of these mutant enzymes, the Met^{20} loop adopts an increasingly open and disordered conformation as a function of the mutation (Fig. 1) (16). The analogous ternary complexes for all three mutations of Ile^{14} in *ec*DHFR were crystallized, and their structures were determined (16). In the I14A and I14V mutants, the structures were obtained in the $P2_1$ space group where the Met^{20} loop is observed in a disordered conformation as this conformation is seemingly stabilized by crystal contacts. These structures are rather similar to the analogous WT structures of Sawaya and Kraut (6) in the $C2$ and $P2_1$ space groups. In contrast, the crystal structure of I14G *ec*DHFR was crystallized in the $P2_12_12$ space group where both the Met^{20} loop and the F-G loop, which is in direct contact with the Met^{20} loop (Fig. 1), are partially disordered. It is possible that a transient population of the open conformational state plays a role in the catalytic cycle because the open conformation enables both substrate binding and product release (3, 18–20). However, replacement of a part of the Met^{20} loop (residues 16–19) with a single glycine residue still yields an enzyme that exhibits some catalytic activity (7), suggesting that the loop is not essential for basic catalytic activity. In our previous work, the above mentioned mutant crystal structures with a disordered Met^{20} loop were not used

This work was supported by Israel Science Foundation Grant 2146/15 and United States-Israel Binational Science Foundation Grant 2012340. The authors declare that they have no conflicts of interest with the contents of this article.

This article contains supplemental Figs. S1–S4.

[1] Both authors contributed equally to this work.

[2] To whom correspondence should be addressed. E-mail: majort@biu.ac.il.

[3] The abbreviations used are: *ec*DHFR, *E. coli* dihydrofolate reductase; DAD, donor-acceptor distance; DHF, dihydrofolate; KIE, kinetic isotope effect; QM, quantum mechanics; MM, molecular mechanics; MD, molecular dynamics; PMF, potential of mean force; GS, ground state; TS, transition state; D-H-A, donor-hydrogen-acceptor; W1–3, waters 1–3; RDF, radial distribution function; ζ_{asym}, antisymmetric reactive stretch coordinate; FEP, free energy perturbation.

for modeling purposes as we focused on the closed conformation. Indeed, it is not clear whether the Met^{20} loop plays a role during the hydride transfer step in general (7) and whether it influences the DAD in particular.

In this work, we present free energy profiles along with structural and dynamic analyses for the hydride transfer in WT *ec*DHFR and three of its mutants (I14V, I14A, and I14G). The WT enzyme is treated in a closed conformation as is observed in the ternary complex crystal structure as well as with a disordered Met^{20} loop conformation (6). The mutant enzymes are also constructed in both the closed and disordered Met^{20} loop conformations. To quantify the effect of conformation on chemistry, we used a hybrid quantum mechanics (QM)/molecular mechanics (MM) Hamiltonian especially designed for the DHFR reaction (21). The free energy profiles were obtained from molecular dynamics (MD) umbrella sampling simulations and were compared with available experimental pre-steady-state single-turnover rates (15). Finally, we estimated the pK_a for the N5 position of the folate moiety with the Met^{20} loop in the closed and disordered conformations.

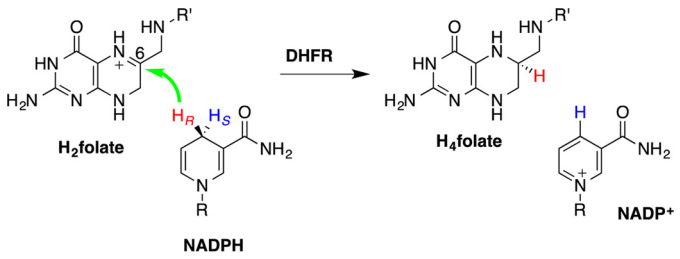

Scheme 1. The DHFR-catalyzed hydride transfer. The *green arrow* marks the transfer of the hydride (H_R) from its donor to the acceptor. *R*, adenine dinucleotide 2′-phosphate; *R*′, *p*-aminobenzoyl-glutamate.

Results

Free energy profiles

We obtained the classical mechanics potential of mean force (PMF) profiles at 25 °C for the catalyzed hydride transfer from NADPH to $H_3folate^+$ (N5-protonated DHF) in the WT *ec*DHFR and three I14*X* mutant *ec*DHFRs, namely I14V, I14A, and I14G. In Fig. 2*A*, we present the PMFs for the WT enzyme as well as for the I14*X* mutant enzymes, all with the Met^{20} loop in the closed conformation. The classical free energy of activation for the WT enzyme, $\Delta G^{\ddagger}$, is 17.4 ± 0.3 kcal/mol, whereas the reaction free energy, ΔG_r, is −4.5 ± 0.3 kcal/mol. The barrier obtained is similar to that obtained in our previous study (16.8 kcal/mol), although the reaction is less exergonic than previously observed (−9.7 kcal/mol) (16, 21). Possible sources for the slight differences are the different initial crystal structures used in the two studies, higher ionic concentration in the

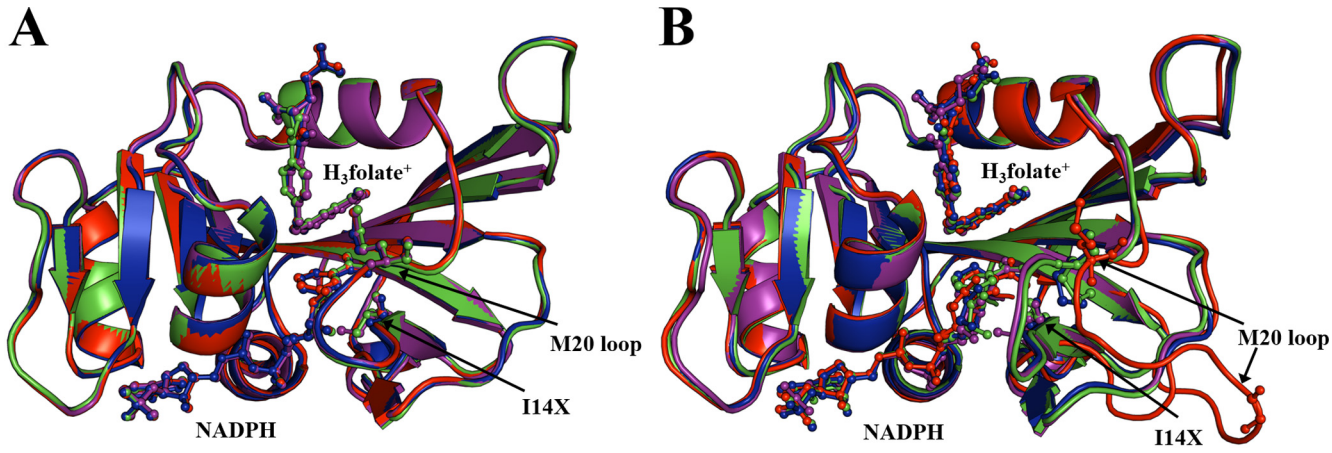

Figure 1. Superimposition of energy-minimized structures of WT *ec*DHFR (*purple*), I14V (*green*), I14A (*blue*), and I14G (*red*) (*A*) and WT* *ec*DHFR (*purple*), I14V* (*green*), I14A* (*blue*), and I14G* (*red*) (*B*).

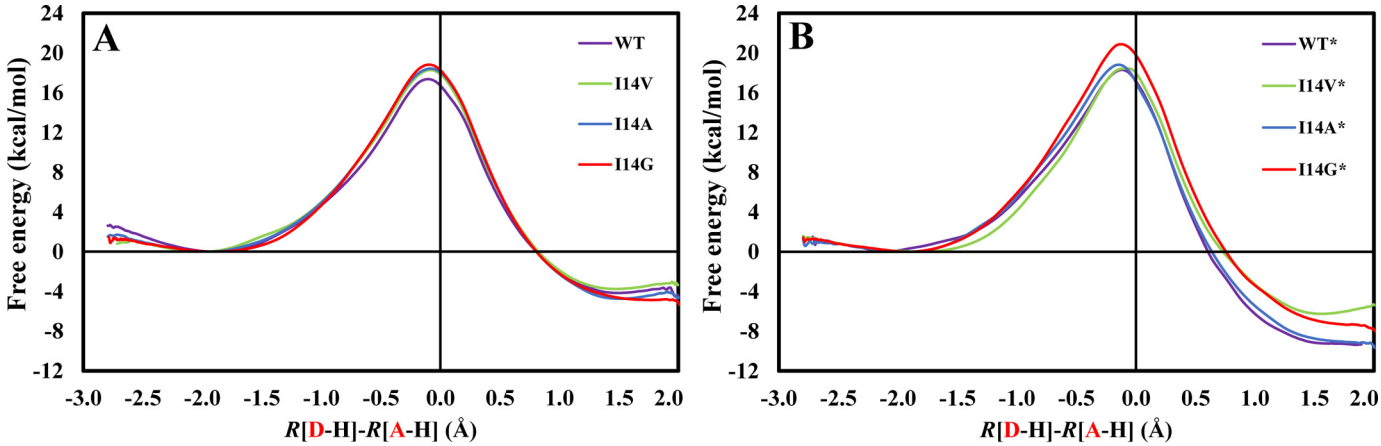

Figure 2. Potential of mean force profiles for WT *ec*DHFR and a series of I14*X* mutants in the closed (*A*) and disordered (*B*) Met^{20} loop conformation.

current work, and statistical uncertainty. We stress that addition of nuclear quantum effects on the hydride transfer typically reduces the barrier for this reaction by 2–3 kcal/mol (21, 22), bringing the computed value into agreement with the phenomenological value estimated from single-turnover rates and the Eyring equation (13.4–14.3 kcal/mol) (15, 23–25). We have previously shown that the nuclear quantum effects are similar for WT and the I14*X* mutants (16, 22). The presence of a slightly less bulky side chain in the I14V *ec*DHFR system causes an increase in the free energy barrier (18.3 ± 0.4 kcal/mol) relative to WT *ec*DHFR in mutant simulations with the Met^{20} loop closed (Figs. 1*A* and 2*A*). Further truncation of the side chain brings about even higher free energy barriers as evident by the $\Delta G^{\ddagger}$ value for the I14A and I14G systems (18.4 ± 0.4 and 18.8 ± 0.4 kcal/mol, respectively). The effect of the mutations is similar to our earlier work and is generally in accord with the experimental trends, although the effect of mutation to Val is slightly overestimated (Table 1) (15–17). We note that the experimental single-turnover rates are pH-dependent and include conformationally induced fit during DHF binding, the protonation at N5, and the hydride transfer step, whereas the current simulations only account for the hydride transfer step. In Fig. 2*B*, we show an analogous plot but with the Met^{20} loop in a disordered conformation (Fig. 1*B*). A similar trend in the PMFs is seen in these profiles (18.3 ± 0.4, 18.5 ± 0.1, 18.8 ± 0.4, and 20.9 ± 0.4 kcal/mol for WT*, I14V*, I14A*, and I14G*, respectively). The free energy barriers are somewhat higher for all models with the Met^{20} loop in a disordered conformation than with the Met^{20} loop in the ordered conformation (see supplemental Fig. S3). We ascribe this to the greater reorganization cost in climbing from the ground state (GS) to the transition state (TS) required for the more disordered structures. We note that the limited accuracy in our computed free energy barriers (approximately ±0.4 kcal/mol) precludes us from drawing quantitative conclusions regarding possible correlation between the effects of Met^{20} loop conformation and I14*X* mutations, such as additivity or cooperativity.

Table 1

Differences in computed activation free energies, $\Delta\Delta G^{\ddagger}$ (kcal/mol), for WT ecDHFR and I14*X* mutants (*X* = Val, Ala, Gly) relative to the WT with the Met^{20} loop in the closed conformation at 25 °C

The enzyme models were constructed with the Met^{20} loop either closed or disordered. The corresponding free energy barriers are compared with relative experimental pre-steady state single-turnover data at 25 °C. Calc., calculated; Exp., experimental.

	$\Delta\Delta G^{\ddagger}$ (kcal/mol)		
	Calc.		
Enzyme	Met^{20} closed	Met^{20} disordered	Exp.[a]
WT	0.0	0.9	0.0
I14V	0.9	1.1	1.2
I14A	1.0	1.4	2.2
I14G	1.4	3.5	4.1

[a] From Ref. 15.

Structural analysis

Conformational substates—We examined different loop conformations that are sampled in each of the simulations using substate analyses. This was done by calculating the backbone dihedral angles of Met^{20} loop residues (Glu^{17} and Met^{20}) as this can demonstrate the conformational flexibility in the loop. The dihedral angles, φ and ψ, of Glu^{17} show distinct Met^{20} loop conformations for the closed and disordered state proteins (Fig. 3). These observations are consistent with those reported by Rod *et al.* (26). In the closed state protein, we note a clear clustering of φ/ψ values near 50°/50°, and these angles do not vary due to the I14*X* mutations as the H-bond between Asp^{122} and Glu^{17} was maintained in the closed state of Met^{20} loop. However, in the disordered Met^{20} conformation, the Asp^{122} and Glu^{17} contacts are lost, and the enzyme adopts another distinct conformation with dihedral values clustered near −20°/−70°. This conformation is similar to the open conformation

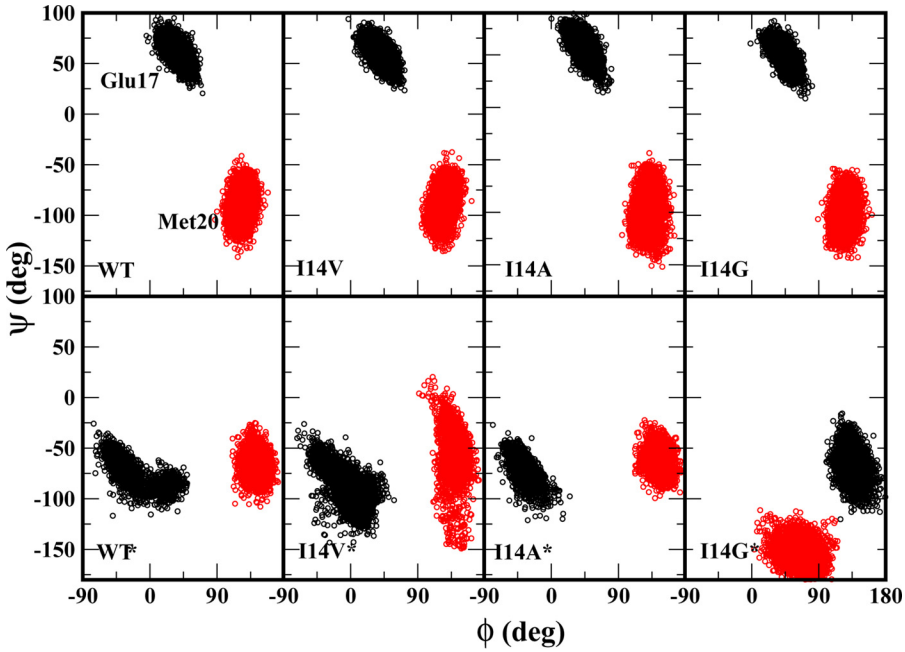

Figure 3. Distribution of backbone dihedral angles φ and ψ for *ec*DHFR residues Glu^{17} and Met^{20} (colored *black* and *red*, respectively). The *upper panel* shows WT and I14*X* mutants in a closed state, and the *bottom panel* represents enzymes with disordered Met^{20} conformations.

Table 2

Ensemble-averaged structural properties of WT DHFR and I14X mutants with the Met^{20} loop in a closed conformation at 25 °C in the ground and transition states

Standard deviations are shown in parentheses. The ensemble-averaged data were obtained from 250-ps simulations of the GS and TS. The position of the TS along the reaction coordinate was determined from the position of the maximum PMF value.

	WT		I14V		I14A		I14G	
	GS	TS	GS	TS	GS	TS	GS	TS
ζ_{asym} (Å)[a]	−1.73 (0.28)	−0.09 (0.01)	−1.98 (0.29)	−0.09 (0.01)	−1.98 (0.33)	−0.10 (0.01)	−1.88 (0.24)	−0.09 (0.01)
C4N–C6 (DAD) (Å)	3.82 (0.21)	2.64 (0.07)	4.02 (0.21)	2.63 (0.07)	4.00 (0.21)	2.65 (0.07)	3.84 (0.23)	2.65 (0.07)
C4N–H4N–C6 (∡D-H-A) (°)	145.09 (15.33)	157.46 (7.69)	140.27 (13.87)	155.09 (7.97)	133.77 (15.58)	157.20 (7.94)	142.15 (17.68)	156.70 (7.75)
N5–S(Met^{20}) (Å)	3.79 (0.34)	3.70 (0.37)	3.90 (0.33)	3.58 (0.29)	3.82 (0.28)	4.16 (0.44)	4.37 (0.56)	3.78 (0.44)
N7N–S(Met^{20}) (Å)	3.67 (0.33)	3.72 (0.33)	3.60 (0.26)	3.71 (0.31)	4.09 (0.45)	4.45 (0.44)	4.66 (0.73)	4.10 (0.61)
N7N–O(Ala^{7}) (Å)	2.78 (0.14)	2.82 (0.13)	2.88 (0.16)	2.90 (0.14)	2.84 (0.13)	2.84 (0.13)	2.91 (0.18)	2.87 (0.14)
N7N–O(Ile^{14}) (Å)	3.02 (0.24)	2.93 (0.22)	3.07 (0.22)	3.13 (0.25)	3.20 (0.32)	3.15 (0.33)	3.21 (0.37)	2.93 (0.18)
O7N–N(Ala^{7}) (Å)	3.19 (0.23)	2.90 (0.11)	3.41 (0.29)	2.92 (0.12)	3.15 (0.18)	2.99 (0.14)	3.30 (0.25)	2.99 (0.14)
N3–Oδ2(Asp^{27}) (Å)	2.73 (0.17)	2.74 (0.17)	2.96 (0.26)	2.86 (0.18)	2.87 (0.20)	2.85 (0.16)	2.91 (0.22)	2.84 (0.17)
NA2–Oδ1(Asp^{27}) (Å)	2.72 (0.11)	2.75 (0.12)	2.79 (0.12)	2.81 (0.12)	2.78 (0.11)	2.78 (0.11)	2.78 (0.11)	2.80 (0.12)

[a] Determined from the stationary points along the PMF profile.

Table 3

Ensemble-averaged structural properties of WT DHFR and I14X mutants with the Met^{20} loop in a disordered conformation at 25 °C in the ground and transition states

Standard deviations are shown in parentheses. The ensemble-averaged data were obtained from 250-ps simulations of the GS and TS. The position of the TS along the reaction coordinate was determined from the position of the maximum PMF value.

	WT*		I14V*		I14A*		I14G*	
	GS	TS	GS	TS	GS	TS	GS	TS
ζ_{asym} (Å)[a]	−2.09 (0.38)	−0.13 (0.01)	−1.77 (0.63)	−0.05 (0.01)	−2.02 (0.26)	−0.16 (0.01)	−1.88 (0.40)	−0.12 (0.01)
C4N–C6 (DAD) (Å)	5.28 (0.32)	2.65 (0.07)	4.74 (0.44)	2.65 (0.07)	3.90 (0.24)	2.65 (0.07)	3.97 (0.26)	2.64 (0.07)
C4N–H4N–C6 (∡D-H-A) (°)	112.95 (10.99)	157.99 (7.97)	108.67 (18.26)	156.91 (7.54)	148.71 (14.93)	157.93 (7.92)	130.60 (21.18)	152.71 (7.29)
N5–S(Met^{20}) (Å)	10.18 (0.71)	9.97 (0.93)	8.90 (0.69)	8.03 (0.83)	8.29 (0.83)	9.07 (0.45)	7.16 (0.77)	15.00 (0.69)
N7N–S(Met^{20}) (Å)	6.90 (0.82)	6.99 (0.82)	7.10 (1.15)	4.67 (0.49)	5.27 (0.52)	5.29 (0.47)	10.75 (0.77)	15.88 (0.74)
N7N–O(Ala^{7}) (Å)	6.09 (0.50)	3.34 (0.38)	4.61 (0.67)	2.94 (0.20)	2.88 (0.14)	3.15 (0.55)	3.12 (0.26)	3.08 (0.20)
N7N–O(Ile^{14}) (Å)	4.08 (0.75)	4.71 (0.44)	4.65 (1.03)	3.09 (0.29)	3.20 (0.33)	3.43 (0.47)	18.61 (0.45)	18.64 (0.48)
O7N–N(Ala^{7}) (Å)	5.97 (0.35)	3.06 (0.19)	5.62 (0.89)	2.94 (0.12)	3.16 (0.26)	3.23 (0.75)	3.05 (0.17)	2.95 (0.13)
N3–Oδ2(Asp^{27}) (Å)	3.17 (0.35)	2.91 (0.18)	2.94 (0.21)	2.84 (0.14)	2.94 (0.20)	2.88 (0.17)	2.87 (0.16)	2.86 (0.15)
NA2–Oδ1(Asp^{27}) (Å)	2.80 (0.13)	2.78 (0.11)	2.79 (0.12)	2.80 (0.12)	2.78 (0.12)	2.77 (0.11)	2.77 (0.11)	2.82 (0.12)

[a] Determined from the stationary points along the PMF profile.

reported by Rod *et al.* (26). In the I14G* mutant, the Met^{20} loop is highly disordered with a wide distribution of φ/ψ angles.

The impact of Met^{20} on structure—The position of the GS stationary point of the PMF along the antisymmetric stretch coordinate for the WT enzyme in the closed conformation is approximately −1.8 Å, whereas for all other systems studied herein the value is greater, approximately −2.0 Å (Tables 2 and 3). There is, however, greater variability in the positions of the GS and TS for the mutant systems with a disordered Met^{20} loop relative to the WT enzyme. For instance, the position of the TS ranges from −0.09 to −0.10 Å for the I14*X* systems (Table 2), whereas for the I14*X** mutants the TS ranges from −0.05 to −0.16 Å (Table 3). Interestingly, the ensemble-averaged value of the DAD distance at the classical TS is nearly identical (2.63–2.66 Å) for all simulations. This invariability of the TS position with mutations is in agreement with earlier findings in our group (16, 27) and many other groups (28–34). However, the DADs in the GS show greater variability for the disordered structures than for the closed structures. The ensemble averaged D-H-A angle in the GS is rather similar for all systems with a closed Met^{20} loop, ranging from 134–145°, whereas this range is widened to 109–149° in the disordered loop enzymes. However, ∡D-H-A at the TS is similar for all systems, ranging from 153 to 158° with similar standard deviations.

In accordance with MD simulations of the GS in Ref. 15, the interaction between the pterin ring and Asp^{27} remains tight throughout the reaction for all systems. Similarly, the hydrogen bonds between the nicotinamide carboxamide moiety and the amide backbone of Ala^{7} and Ile^{14} remain intact for all systems except for I14G*. In this latter system, a different binding mode is observed in the crystal structure where the carboxamide group interacts with the backbone of Thr^{123} instead of Ile^{14}. Additionally, the WT enzyme with the closed Met^{20} loop conformation has the tightest hydrogen bonds to the cofactor and substrate at the TS. The greatest difference in the interaction pattern between the WT/I14*X* and WT*/I14*X** mutant systems is found in the contact between the Met^{20} residue and the substrate–cofactor complex (Fig. 1). In the WT and I14*X* systems, the Met^{20} loop packs against the reactive complex. This is reflected in the distances between the Met^{20} sulfur atom and key nitrogen atoms in the NAD(H) and pterin moieties that range between 3.6 and 4.7 Å (Tables 2 and 3). In contrast, in the WT* and I14*X** systems, the Met^{20} loop is not packed against the pterin ring, and the range of Met^{20}-nitrogen distances is 4.7–15.9 Å.

An additional interesting structural aspect that is greatly influenced by the conformation of the Met^{20} loop is the active site hydration. It is well known that several conserved water molecules are located near the cofactor–substrate complex (6, 35–38). Particular attention has been devoted to the water molecule likely responsible for the N5 protonation (38). Here we focus on a triad of waters that are located near the pterin ring O4 oxygen and Asp^{27} (W1–3; Fig. 4) whose detailed structure has been revealed by a high-resolution WT *ec*DHFR structure (38). These water molecules stabilize the reduced pterin and

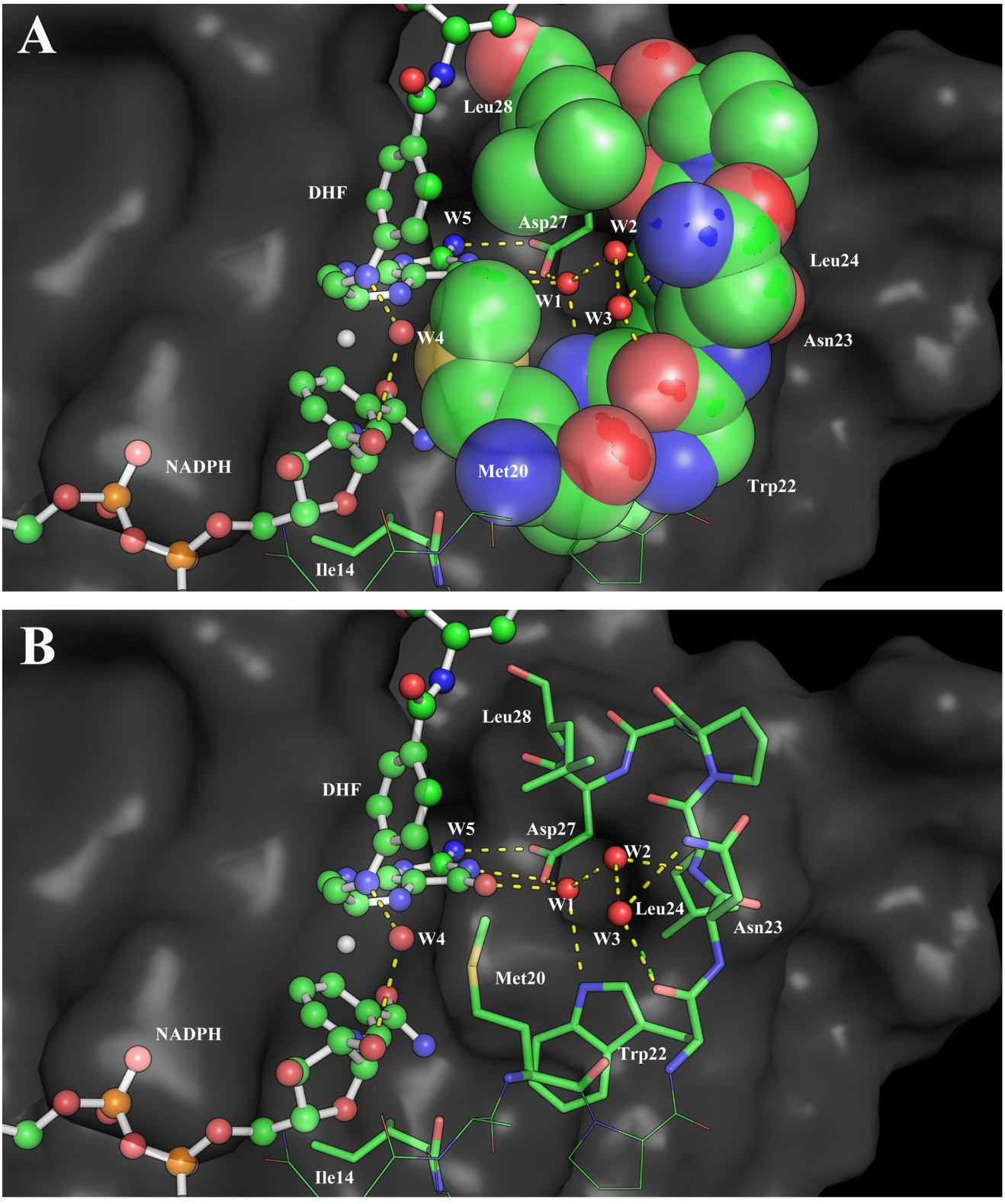

Figure 4. A snapshot of TS configuration of WT *ec*DHFR from molecular dynamics simulations. Water cavity-forming residues are shown as space-filling (*A*) and stick (*B*) models.

likely give greater weight to the polarized resonance structures (Scheme 2) (39, 40). These resonance structures facilitate charge–charge interactions with Asp^{27}. Indeed, Garcia-Viloca *et al.* (40) found that this resonance-assisted charge-separated moiety (Scheme 2) is the most polarized region of the substrate–cofactor entity. In Fig. 5, we present the radial distribution functions (RDFs) around O4 of the pterin ring in the GS and at the TS for all enzyme forms studied herein. There is a striking difference in the RDFs for the closed and disordered Met^{20} loop forms. In the closed enzyme, there are distinct peaks

Scheme 2. Possible resonance structures for the pterin ring in H_4folate. *R′*, *p*-aminobenzoyl-glutamate.

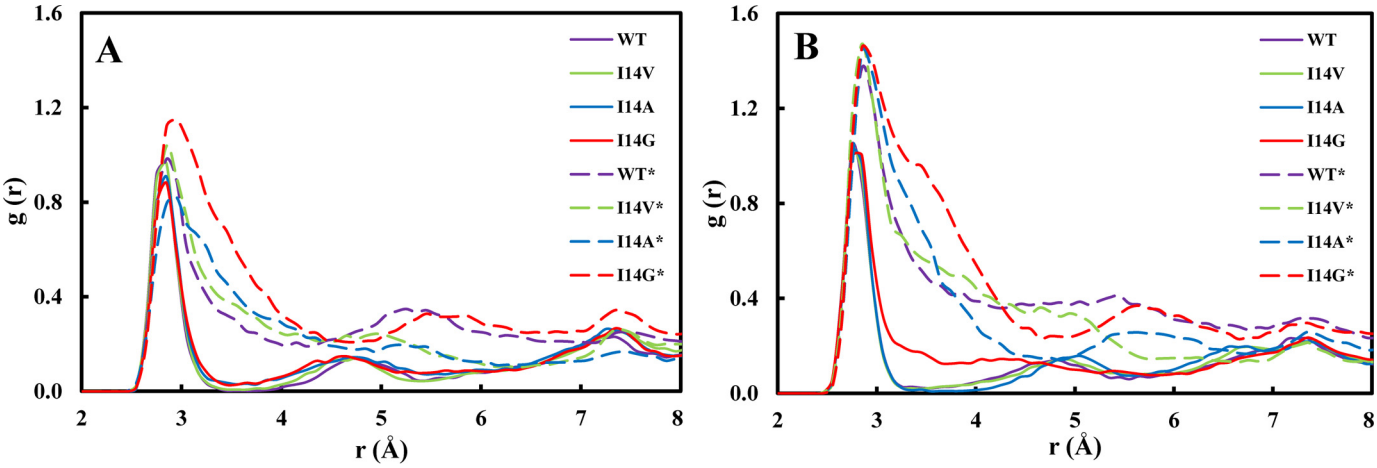

Figure 5. Hydration radial distribution functions near the O4 oxygen of the pterin ring in the active site of *ec*DHFR. *A*, ground state. *B*, transition state.

with the first solvation shell corresponding to a highly organized water molecule. The maximum of this peak is located at ~2.85 Å and corresponds to a water molecule that interacts with O4, Asp^{27}, and Trp^{22} (W1) and is highly conserved in DHFRs (Fig. 4). This water molecule is not exchanged throughout the simulations. A second peak in the RDFs is located at ~4.6 Å, and a third peak is found at ~7.5 Å, corresponding to the two water molecules W2 and W3 (see supplemental Fig. S4). In the simulations with the disordered Met^{20} loop, the RDFs are much broader, suggesting less hydration structure with considerably more waters penetrating the active site. However, even in the case of the open Met^{20} loop simulations, a water molecule is directly interacting with O4. Inspection of the identity of the water molecule closest to O4 revealed that in the open Met^{20} loop simulations this water molecule is exchangeable. Notably, in the GS of the I14G* simulations, the maximum peak is shifted to 2.95 Å, suggesting a more disordered state. For the WT enzyme with a closed Met^{20} loop at the TS, the maximum peak of the first hydration shell is shifted to 2.75 Å, suggesting TS stabilization.

The impact of Met^{20} on N5 pK_a—We examined the pK_a of substrate N5 atom in the ternary Michaelis complex. Our calculated pK_a for the closed (WT) and disordered (WT*) state enzyme are 8.3 and 6.8, respectively, in excellent agreement with the values determined by Brooks and co-workers (14, 41).The pK_a obtained for the less ordered conformation (6.8) is similar to the experimentally reported pK_a (~6.5 (42) or 6.7 (43)), suggesting that protonation occurs in a conformational state with the Met^{20} loop accessible to bulk water. In contrast, the pK_a of N5 in the closed Met^{20} conformation is observed to be less acidic (pK_a = 8.3), which is consistent with the recent experimental study by Liu *et al.* (43) These authors found DHF N5 to be partially protonated at pH values up to 11 based on kinetic studies (43). These kinetic studies showed that hydride transfer occurs even at such high pH values. Considering that in the current work we have established that hydride transfer occurs in the closed Met^{20} loop state, we suggest that the elevated pK_a value reported by Liu *et al.* (43) corresponds to the closed Met^{20} loop state. The role of Met^{20} in modulating the N5 pK_a has been emphasized previously by Brooks and co-workers (14, 41), and the current findings fully support their findings. We suggest that different Met^{20} loop conformations bring about changes to the active site electrostatics that might affect N5 acidity. Specifically, these changes are expected to be correlated with the active site hydration as will be shown below.

Next, we analyzed the hydration near DHF in the closed and disordered Met^{20} conformations as well as in bulk water. We plotted the radial distribution function between the substrate N5 and the water oxygens for the two folate forms, *i.e.* H_3F^+ and H_2F (Fig. 6). The broad peaks near the H_3F^+ N5 (2.95 Å) in solution and WT* enzyme indicate specific hydration (Fig. 6*A*). In the closed WT complex, the Met^{20} side chain packs against the pterin ring of the substrate (6, 10, 44, 45), and no first solvation shell is observed. A small peak near 5.5 Å in both ternary complexes represents a water molecule stabilized by Asp^{27} and H_3F^+ O4 interactions. In Fig. 6*B*, a sharp peak is observed at 2.85 Å, which shows that water tends to stabilize near N5 of H_2F via hydrogen bond interactions in all the systems. The Met^{20} loop flexibility has been suggested to be responsible for allowing water access to the substrate. Interestingly, in crystal structures of the ternary complex of *ec*DHFR, a water molecule is also observed near N5 of H_2F (38). Seemingly, prior to N5 protonation, the packing of the Met^{20} loop is somewhat loose, allowing access to water, whereas following N5 protonation the packing is tightened in preparation for the hydride transfer step, thereby excluding water molecules and hence raising the N5 pK_a.

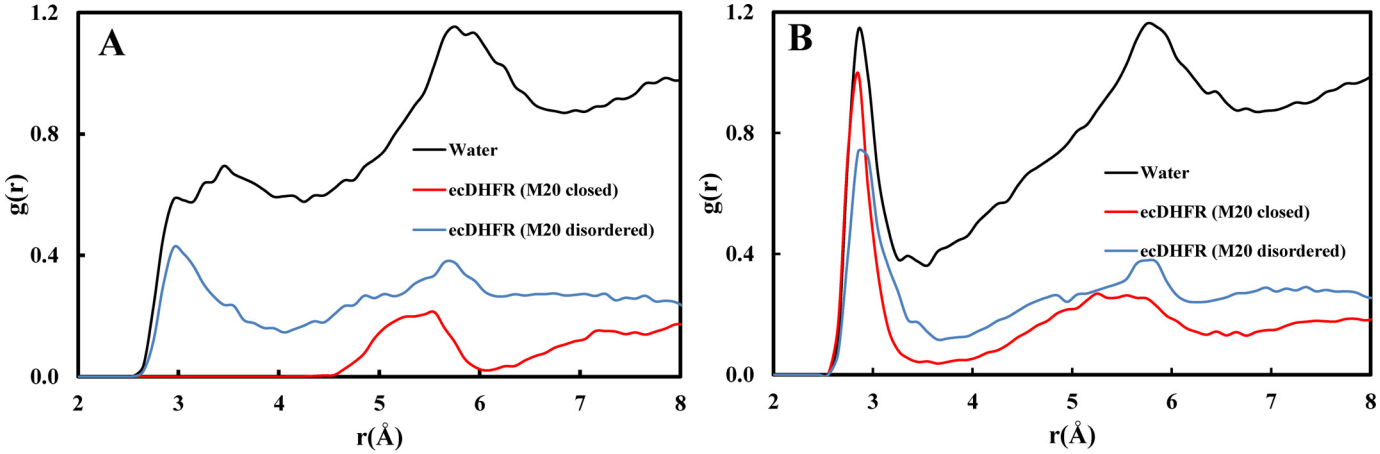

Figure 6. Radial distribution functions between the N5 atom of the pterin ring and water oxygens in solution and ternary complex at the end points of the physical states. *A*, H_3F^+. *B*, H_2F. Substrate in solution colored as *black* and ternary *ec*DHFR complexes with the closed and disordered Met^{20} loop conformations colored as *red* and *blue*, respectively.

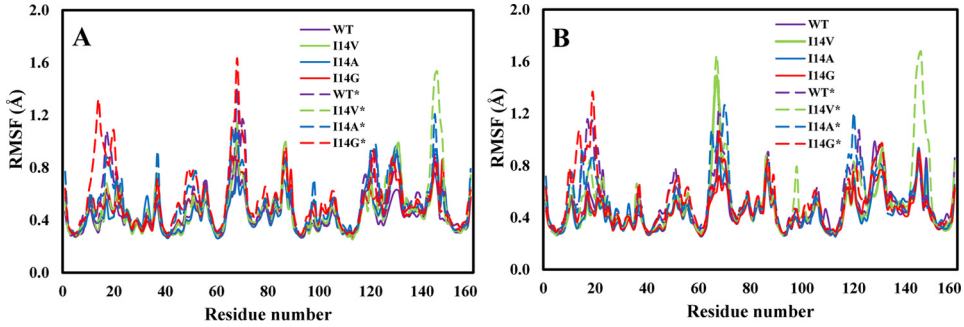

Figure 7. Root mean square fluctuations (*RMSF*) of Cα atoms of *ec*DHFR in the ground state (*A*) and transition state (*B*).

The impact of Met^{20} on dynamics—In Fig. 7, we present the root mean square fluctuations of the Cα atoms as a function of amino acid residue number in the GS and TS for WT and I14*X* mutant enzyme forms in the closed and disordered Met^{20} loop conformations. The main characteristic that is apparent in the root mean square fluctuation plots is the increased flexibility in the systems with the disordered Met^{20} loop. In particular, the Met^{20} loop (residues 9–23) and F-G loop (residues 117–131) regions are considerably more flexible in the disordered than in the closed structures. This is likely due to changes in the contact between these two segments in the disordered structures. For instance, the contact between the side chain of Asp^{122} in the F-G loop and the backbone amide of Glu^{17} in the Met^{20} loop is lost. We also note increased flexibility in the C-D loop (residues 64–71) for all the disordered systems, including the WT* enzyme. These fluctuations are slightly greater in some of the mutants. Finally, we note that there is great flexibility in Gln^{146} in the I14V* mutant in the disordered conformation. This greater fluctuation in the I14V* mutant is the result of the loss of an intraloop hydrogen bond between Asp^{144} and Gln^{146} during the simulation. The general observations discussed above are in agreement with earlier experimental and theoretical studies (11, 46).

Discussion

A crucial question regarding the chemical steps in enzyme reactions is to what extent global protein motions might participate in the reaction coordinate. In the case of *ec*DHFR, it has been argued that the Met^{20} loop participates in the reaction coordinate. In the current study, we asked an even simpler question: whether the Met^{20} loop is preferably closed during hydride transfer or not and whether this influences the DADs. Seemingly, based on the free energy profiles obtained in this work, the Met^{20} loop is indeed likely to be in the closed conformation in the WT enzyme with the Met^{20} residue packed against the pterin ring. In the case of the WT enzyme, we simulated both the closed and disordered Met^{20} loop configurations and obtained a slightly higher free energy barrier with the disordered Met^{20} loop ($\Delta\Delta G^{\ddagger} \sim 1$ kcal/mol). In the case of the I14*X* mutants (*X* = Val, Ala, Gly), we obtained best agreement with pre-steady-state single-turnover rates using the more disordered structures (Table 1), although the results are within statistical error for *X* = Val, Ala. A possible interpretation of these results is that the Met^{20} loop in general and the Met^{20} amino acid in particular are preferentially in the closed conformation during the hydride transfer step in WT *ec*DHFR but not necessarily so in the I14*X* mutants. That is, the I14*X* mutants can reach a reactive configuration similar to that of the WT enzyme but with a more disordered Met^{20} loop. We note, however, that the effect of the Met^{20} loop is small in agreement with experiments showing that the enzyme is active with significant parts of the Met^{20} loop deleted (7). We did not observe any strong connection between the Met^{20} loop conformation and the DADs.

Our simulations verify earlier results of Brooks and co-workers (41) relating to the crucial role of the Met^{20} loop in determining the substrate N5 pK_a. The pK_a value computed for the disordered Met^{20} loop (~6.8) is comparable with the experimentally determined value (~6.5 (42) or 6.7 (43)), whereas the pK_a computed for the closed conformation (8.3) is in agreement with the finding that hydride transfer occurs at basic pH values up to ~11 (43). The difference in pK_a values for the two loop conformations is likely due to differences in active site hydration.

Additionally, the closed Met^{20} loop conformation is also involved in ordering in the structure of several conserved water molecules in the vicinity of the pterin ring O4 position. It has been suggested previously that these water molecules are part of a proton relay (36, 37) or ligand recognition (6, 35, 38); here we suggest that these water molecules also play a classical enzyme catalytic role, TS stabilization. Indeed, these tightly bound waters likely facilitate substrate polarization as suggested by Garcia-Viloca *et al.* (40) and stabilize charge separation (Scheme 2). This in turn enhances substrate binding via interaction with Asp^{27} and serves to mitigate hydride charge transfer by screening the Asp^{27} charge (Fig. 4). Experimentally, mutation of Trp^{22}, which forms part of this hydration motif, to His or Phe results in a non-negligible reduction in the rate of the hydride transfer step as determined by stopped flow kinetics (47). In the case of other DHFRs, this could be a similar requirement, such as in human DHFR where, instead of the Met^{20} residue, Leu^{22} is packed against the substrate–cofactor complex and creates a similar water cavity.

Conclusions

A question concerning the catalytic cycle of *ec*DHFR that has garnered significant interest is whether the Met^{20} loop motion is coupled to the hydride transfer step. In the current study, we examined whether the Met^{20} loop is preferably closed during hydride transfer or not and whether this influences the DADs. To address this question, we studied the WT and three mutant forms (I14*X*; *X* = Val, Ala, Gly) of the enzyme and compared the finding with published experimental observations. These enzyme forms were modeled with the Met^{20} loop in its closed and disordered conformations. Using hybrid QM/MM free energy simulations, we obtained optimal agreement with experimental pre-steady-state kinetics modeling the WT in the closed Met^{20} form and the mutants in the disordered Met^{20} form. Indeed, we found that the disordered conformation of the Met^{20} loop causes a consistent slight increase in the activation free energy barrier for the WT and mutant enzymes. We conclude that a closed Met^{20} loop is likely preferential for catalysis as it aids in the preorganization of several conserved water molecules, likely influencing both ligand binding and TS stabilization. The DADs at the TS, however, remain rather similar in the closed and disordered conformations. We also found a significant correlation between the substrate N5 pK_a and the Met^{20} conformation. The open Met^{20} loop conformation facilitates protonation prior to the hydride transfer. Closing of this loop reduces the acidity of the N5 proton, thereby stabilizing the H_3F^+ state in preparation for hydride transfer.

Materials and methods

The X-ray crystal structures of WT *ec*DHFR (Protein Data Bank codes 4RGC and 1RB2) (6, 38) and mutant *E. coli* I14V, I14A, and I14G (Protein Data Bank codes 4QLG, 4QLE, and 4QLF, respectively) (16) with folate and the oxidized cofactor $NADP^+$ were used to construct the initial configurations for the present study. The 4RGC structure corresponds to the closed ternary complex where the Met^{20} residue is packed against folate (henceforth WT), whereas in 1RB2 the Met^{20} loop is disordered (henceforth WT*; * = disordered). The crystal structure of I14G was missing a part of the cofactor and part of a loop (residues 122 and 123). The missing cofactor coordinates were obtained by superimposing the I14V structure on the I14G structure followed by extraction of the missing coordinates for I14G from I14V. The missing residues were modeled with Discovery Studio software (Biovia, Inc.). These mutant enzyme forms that have the Met^{20} loop in a disordered conformation are termed I14*X** (*X* = Val, Ala, Gly and * = disordered). Additionally, a second set of mutant structures that are similar to the WT were constructed *in silico* by changing the Ile^{14} residue in the original WT *ec*DHFR structure (Protein Data Bank code 4RGC) to Val, Ala, or Gly (termed I14*X* where *X* = Val, Ala, Gly).

The setup and MD heating and equilibration simulations of all systems were carried out using procedures similar to those used for the WT and mutant *ec*DHFRs in previous studies (16, 21, 48). Briefly, the protonation states of all polar amino acid residue side chains were adjusted to pH 7, and the protonation states of the His residues (either neutral tautomeric forms or positively charged form) were determined based on the hydrogen bonding patterns of the local environment. The N5 position of the pterin ring of the dihydrofolate was protonated (43, 49, 50). The HBUILD facility in the program CHARMM was used to add hydrogen atoms (51, 52). 29 sodium ions and 15 chlorine ions were added to all enzyme systems to neutralize the overall negative charge. This ionic concentration mimics experimental conditions (16) and effectively screens the charges in the system.

The potential energy surface in the current study is described by a hybrid QM/MM Hamiltonian (53) where the QM region is treated by a modified AM1 semiempirical Hamiltonian (54) denoted AM1-specific reaction parameter (55). This Hamiltonian was designed to reproduce high-level calculations for an assortment of electronic and thermodynamic properties for reactions involving various nicotinamide and pterin derivatives (21). The QM region includes significant fragments of DHF and NADPH, which are proximal to the reaction center, whereas the MM region contains the remaining ligand atoms, the entire protein, water molecules, and salt. The water molecules were represented by the three-point charge TIP3P model (56). Hydrogen link atoms were placed across the bonds intersecting the QM/MM boundary. The QM/MM interactions were treated by electrostatic embedding. A detailed QM/MM partitioning scheme and a thorough description of the development of the AM1-specific reaction parameter Hamiltonian are provided elsewhere (21). In modeling the MM region, we used the all-atom CHARMM36 force field (57–60).

Periodic boundary conditions were used to solvate the Michaelis complex using a pre-equilibrated cubic water box (~65 × ~65 × ~65 Å) while treating long-range electrostatic interactions with the Ewald summation technique (64 × 64 × 64 fast Fourier transform grid, $\kappa = 0.340$ Å^{-1}) (61). All systems were fully minimized, heated up gradually to 298 K for 25 ps, and equilibrated at that temperature for 1 ns. All equilibrations were conducted in the isothermal-isobaric (NPT) ensemble at 1 atm, and the target temperature was controlled by the extended constant pressure/temperature method (62, 63) and a Hoover thermostat (64). The leapfrog integration scheme (65) was used to propagate the equations of motions, and the SHAKE algorithm (66) was applied to constrain all MM bonds involving hydrogen atoms, allowing a time step of 1 fs. During the initial stages of the equilibration, several nuclear Overhauser effect (NOE) restraints were imposed on key hydrogen bond interactions between the ligands and the surrounding residues as well as within the protein.

The umbrella sampling technique (67) was used to determine the classical-mechanical PMF for the hydride transfer reaction at 25 °C (*i.e.* the free energy profile along a predefined reaction coordinate). The reaction coordinate was defined as the antisymmetric reactive stretch coordinate, ζ_{asym}. Specifically, ζ_{asym} is defined as the difference between the lengths of the breaking C4N–H and forming H–C6 bonds. The reaction coordinate was discretized and divided into 16 evenly spaced regions, or "windows," ranging from −2.00 to 1.5 Å. Each window was subjected to an appropriate harmonic restraint, which keeps ζ_{asym} in the desired region, and an umbrella potential (roughly the negative of the PMF) as a function of ζ_{asym}. The cumulative simulation time per window was 1 ns, and the statistics for the reaction coordinate were sorted into bins of width 0.01 Å. PMF profiles were computed using the weighted histogram analysis method (48, 68). The statistical error was estimated using the bootstrapping algorithm (1000 steps) combined with the weighted histogram analysis method (69). The resulting error analysis of the free energy profiles obtained is provided in the supplemental Fig. S1. The effect of bin size on the free energy profiles was also investigated (supplemental Fig. S2). We also plotted the free energy profiles computed for different time intervals in the same figure.

To evaluate the pK_a for H_2F at the N5 position, we carried out free energy perturbation (FEP) simulations of substrate molecule in bulk water and in two ternary complexes of the WT *ec*DHFR (with closed and disordered Met^{20} loops). We used single-topology FEP QM/MM simulations where a molecule is transformed from one chemical state to another via a series of intermediates (70, 71). We used the λ-dynamics methodology where the potential energy function of system is defined as follows.

$$U(\lambda) = (1 - \lambda)U_A + \lambda U_B \qquad \text{(Eq. 1)}$$

The *A* and *B* states here correspond to the protonated substrate H_3F^+ and its unprotonated analog H_2F, respectively, and λ is a coupling parameter. This approach entails annihilating the QM and classical force field terms for the proton attached to the DHF N5 position as a function of λ. In the present study, we chose $\Delta\lambda = 0.1$, and 10 windows were used to perturb $\lambda = 0 \rightarrow 0.1 \rightarrow 0.2 \ldots \rightarrow 1.0$. The cumulative simulation time per window was 1 ns. The double-wide sampling used here includes the FEP calculations in both forward and reverse directions. Therefore, for each sampling window (λ), the free energies for the forward and backward perturbations were obtained. We confirmed the convergence of these simulations by comparing the backward and forward perturbation free energies for each λ window. Finally, the protonation free energies for the full reaction were obtained by integrating all the sampling windows (λ).

The difference between the substrate protonation free energy in the enzyme and solution was used to compute the pK_a shift for each complex relative to that in bulk water (72). To compute estimates for the experimental pK_a values in the complexes, we added the corresponding computed ΔpK_a shift to the experimental pK_a value in bulk water (2.6) (41, 73).

Author contributions—D. T. M. designed and coordinated the study and wrote the paper. A. R. M. and A. V.-K. performed and analyzed the simulations. A. K. contributed to interpretation of the data and wrote the paper. All authors reviewed the results and approved the final version of the manuscript.

References

1. Francis, K., and Kohen, A. (2016) Dihydrofolate reductase as a model for enzyme catalysis. *Curr. Biotechnol.* **4,** 77–86
2. McElheny, D., Schnell, J. R., Lansing, J. C., Dyson, H. J., and Wright, P. E. (2005) Defining the role of active-site loop fluctuations in dihydrofolate reductase catalysis. *Proc. Natl. Acad. Sci. U.S.A.* **102,** 5032–5037
3. Bhabha, G., Lee, J., Ekiert, D. C., Gam, J., Wilson, I. A., Dyson, H. J., Benkovic, S. J., and Wright, P. E. (2011) A dynamic knockout reveals that conformational fluctuations influence the chemical step of enzyme catalysis. *Science* **332,** 234–238
4. Loveridge, E. J., Behiry, E. M., Guo, J., and Allemann, R. K. (2012) Evidence that a 'dynamic knockout' in Escherichia coli dihydrofolate reductase does not affect the chemical step of catalysis. *Nat. Chem.* **4,** 292–297
5. Kohen, A. (2015) Role of dynamics in enzyme catalysis: substantial vs. semantic controversies. *Acc. Chem. Res.* **48,** 466–473
6. Sawaya, M. R., and Kraut, J. (1997) Loop and subdomain movements in the mechanism of *Escherichia coli* dihydrofolate reductase: crystallographic evidence. *Biochemistry* **36,** 586–603
7. Li, L., Falzone, C. J., Wright, P. E., and Benkovic, S. J. (1992) Functional role of a mobile loop of *Escherichia coli* dihydrofolate reductase in transition-state stabilization. *Biochemistry* **31,** 7826–7833
8. Venkitakrishnan, R. P., Zaborowski, E., McElheny, D., Benkovic, S. J., Dyson, H. J., and Wright, P. E. (2004) Conformational changes in the active site loops of dihydrofolate reductase during the catalytic cycle. *Biochemistry* **43,** 16046–16055
9. Osborne, M. J., Schnell, J., Benkovic, S. J., Dyson, H. J., and Wright, P. E. (2001) Backbone dynamics in dihydrofolate reductase complexes: role of loop flexibility in the catalytic mechanism. *Biochemistry* **40,** 9846–9859
10. Schnell, J. R., Dyson, H. J., and Wright, P. E. (2004) Effect of cofactor binding and loop conformation on side chain methyl dynamics in dihydrofolate reductase. *Biochemistry* **43,** 374–383
11. Boehr, D. D., McElheny, D., Dyson, H. J., and Wright, P. E. (2006) The dynamic energy landscape of dihydrofolate reductase catalysis. *Science* **313,** 1638–1642
12. Thorpe, I. F., and Brooks, C. L., III. (2003) Barriers to hydride transfer in wild type and mutant dihydrofolate reductase from *E. coli*. *J. Phys. Chem. B* **107,** 14042–14051
13. Thorpe, I. F., and Brooks, C. L., 3rd (2005) Conformational substates modulate hydride transfer in dihydrofolate reductase. *J. Am. Chem. Soc.* **127,** 12997–13006

14. Arora, K., and Brooks, C. L., 3rd (2013) Multiple intermediates, diverse conformations, and cooperative conformational changes underlie the catalytic hydride transfer reaction of dihydrofolate reductase. *Top. Curr. Chem.* **337,** 165–187
15. Stojković, V., Perissinotti, L. L., Willmer, D., Benkovic, S. J., and Kohen, A. (2012) Effects of the donor-acceptor distance and dynamics on hydride tunneling in the dihydrofolate reductase catalyzed reaction. *J. Am. Chem. Soc.* **134,** 1738–1745
16. Doron, D., Stojković, V., Gakhar, L., Vardi-Kilshtain, A., Kohen, A., and Major, D. T. (2015) Free energy simulations of active-site mutants of dihydrofolate reductase. *J. Phys. Chem. B* **119,** 906–916
17. Stojkovic, V., Perissinotti, L. L., Lee, J., Benkovic, S. J., and Kohen, A. (2010) The effect of active-site isoleucine to alanine mutation on the DHFR catalyzed hydride-transfer. *Chem. Commun.* **46,** 8974–8976
18. Miller, G. P., and Benkovic, S. J. (1998) Strength of an interloop hydrogen bond determines the kinetic pathway in catalysis by *Escherichia coli* dihydrofolate reductase. *Biochemistry* **37,** 6336–6342
19. Miller, G. P., Wahnon, D. C., and Benkovic, S. J. (2001) Interloop contacts modulate ligand cycling during catalysis by *Escherichia coli* dihydrofolate reductase. *Biochemistry* **40,** 867–875
20. Boehr, D. D., McElheny, D., Dyson, H. J., and Wright, P. E. (2010) Millisecond timescale fluctuations in dihydrofolate reductase are exquisitely sensitive to the bound ligands. *Proc. Natl. Acad. Sci. U.S.A.* **107,** 1373–1378
21. Doron, D., Major, D. T., Kohen, A., Thiel, W., and Wu, X. (2011) Hybrid quantum and classical simulations of the dihydrofolate reductase catalyzed hydride transfer reaction on an accurate semi-empirical potential energy surface. *J. Chem. Theory Comput.* **7,** 3420–3437
22. Major, D. T., Eitan, R., Das, S., Mhashal, A., and Singh, V. (2017) Nuclear quantum effects in enzymatic reactions, in *Simulating Enzyme Reactivity* (Tunon, I., and Moliner, V., eds) pp. 340–374, RCS Publishing, Cambridge, UK
23. Cameron, C. E., and Benkovic, S. J. (1997) Evidence for a functional role of the dynamics of glycine-121 of *Escherichia coli* dihydrofolate reductase obtained from kinetic analysis of a site-directed mutant. *Biochemistry* **36,** 15792–15800
24. Rajagopalan, P. T., Lutz, S., and Benkovic, S. J. (2002) Coupling interactions of distal residues enhance dihydrofolate reductase catalysis: mutational effects on hydride transfer rates. *Biochemistry* **41,** 12618–12628
25. Loveridge, E. J., and Allemann, R. K. (2011) Effect of pH on hydride transfer by *Escherichia coli* dihydrofolate reductase. *ChemBioChem* **12,** 1258–1262
26. Rod, T. H., Radkiewicz, J. L., and Brooks, C. L., 3rd (2003) Correlated motion and the effect of distal mutations in dihydrofolate reductase. *Proc. Natl. Acad. Sci. U.S.A.* **100,** 6980–6985
27. Roston, D., Kohen, A., Doron, D., and Major, D. T. (2014) Simulations of remote mutants of dihydrofolate reductase reveal the nature of a network of residues coupled to hydride transfer. *J. Comput. Chem.* **35,** 1411–1417
28. Garcia-Viloca, M., Truhlar, D. G., and Gao, J. (2003) Reaction-path energetics and kinetics of the hydride transfer reaction catalyzed by dihydrofolate reductase. *Biochemistry* **42,** 13558–13575
29. Fan, Y., Cembran, A., Ma, S., and Gao, J. (2013) Connecting protein conformational dynamics with catalytic function as illustrated in dihydrofolate reductase. *Biochemistry* **52,** 2036–2049
30. Luk, L. Y., Javier Ruiz-Pernía, J., Dawson, W. M., Roca, M., Loveridge, E. J., Glowacki, D. R., Harvey, J. N., Mulholland, A. J., Tuñón, I., Moliner, V., and Allemann, R. K. (2013) Unraveling the role of protein dynamics in dihydrofolate reductase catalysis. *Proc. Natl. Acad. Sci. U.S.A.* **110,** 16344–16349
31. Ruiz-Pernia, J. J., Luk, L. Y., García-Meseguer, R., Martí, S., Loveridge, E. J., Tuñón I., Moliner, V., and Allemann, R. K. (2013) Increased dynamic effects in a catalytically compromised variant of *Escherichia coli* dihydrofolate reductase. *J. Am. Chem. Soc.* **135,** 18689–18696
32. Agarwal, P. K., Billeter, S. R., and Hammes-Schiffer, S. (2002) Nuclear quantum effects and enzyme dynamics in dihydrofolate reductase catalysis. *J. Phys. Chem. B* **106,** 3283–3293
33. Watney, J. B., Agarwal, P. K., and Hammes-Schiffer, S. (2003) Effect of mutation on enzyme motion in dihydrofolate reductase. *J. Am. Chem. Soc.* **125,** 3745–3750
34. Boekelheide, N., Salomón-Ferrer, R., and Miller, T. F., 3rd (2011) Dynamics and dissipation in enzyme catalysis. *Proc. Natl. Acad. Sci. U.S.A.* **108,** 16159–16163
35. Reyes, V. M., Sawaya, M. R., Brown, K. A., and Kraut, J. (1995) Isomorphous crystal structures of *Escherichia coli* dihydrofolate reductase complexed with folate, 5-deazafolate, and 5,10-dideazatetrahydrofolate: mechanistic implications. *Biochemistry* **34,** 2710–2723
36. Lee, H., Reyes, V. M., and Kraut, J. (1996) Crystal structures of *Escherichia coli* dihydrofolate reductase complexed with 5-formyltetrahydrofolate (folinic acid) in two space groups: evidence for enolization of pteridine O4. *Biochemistry* **35,** 7012–7020
37. Miller, G. P., and Benkovic, S. J. (1998) Stretching exercises—flexibility in dihydrofolate reductase catalysis. *Chem. Biol.* **5,** R105–R113
38. Wan, Q., Bennett, B. C., Wilson, M. A., Kovalevsky, A., Langan, P., Howell, E. E., and Dealwis, C. (2014) Toward resolving the catalytic mechanism of dihydrofolate reductase using neutron and ultrahigh-resolution X-ray crystallography. *Proc. Natl. Acad. Sci. U.S.A.* **111,** 18225–18230
39. Cummins, P. L., and Gready, J. E. (1996) Solvent effects in active-site molecular dynamics simulations on the binding of 8-methyI-N5-deazapterin and 8-methylpterin to dihydrofolate reductase. *J. Comput. Chem.* **17,** 1598–1611
40. Garcia-Viloca, M., Truhlar, D. G., and Gao, J. (2003) Importance of substrate and cofactor polarization in the active site of dihydrofolate reductase. *J. Mol. Biol.* **327,** 549–560
41. Khavrutskii, I. V., Price, D. J., Lee, J., and Brooks, C. L., 3rd (2007) Conformational change of the methionine 20 loop of *Escherichia coli* dihydrofolate reductase modulates pK_a of the bound dihydrofolate. *Protein Sci.* **16,** 1087–1100
42. Fierke, C. A., Johnson, K. A., and Benkovic, S. J. (1987) Construction and evaluation of the kinetic scheme associated with dihydrofolate reductase from *Escherichia coli*. *Biochemistry* **26,** 4085–4092
43. Liu, C. T., Francis, K., Layfield, J. P., Huang, X., Hammes-Schiffer, S., Kohen, A., and Benkovic, S. J. (2014) The *Escherichia coli* dihydrofolate reductase catalyzed proton and hydride transfers: order and the roles of Asp27 and Tyr100. *Proc. Natl. Acad. Sci. U.S.A.* **111,** 18231–18236
44. Bystroff, C., Oatley, S. J., and Kraut, J. (1990) Crystal structures of *Escherichia coli* dihydrofolate reductase: the $NADP^+$ holoenzyme and the folate·$NADP^+$ ternary complex. Substrate binding and a model for the transition state. *Biochemistry* **29,** 3263–3277
45. Brown, K. A., and Kraut, J. (1992) Exploring the molecular mechanism of dihydrofolate reductase. *Faraday Discuss.* **93,** 217–224
46. Radkiewicz, J. L., and Brooks, B. R. (2000) Protein dynamics in enzymatic catalysis: exploration of dihydrofolate reductase. *J. Am. Chem. Soc.* **122,** 225–231
47. Warren, M. S., Brown, K. A., Farnum, M. F., Howell, E. E., and Kraut, J. (1991) Investigation of the functional role of tryptophan-22 in *Escherichia coli* dihydrofolate reductase by site-directed mutagenesis. *Biochemistry* **30,** 11092–11103
48. Doron, D., Kohen, A., and Major, D. T. (2012) Collective reaction coordinate for hybrid quantum and molecular mechanics simulations: a case study of the hydride transfer in dihydrofolate reductase. *J. Chem. Theory Comput.* **8,** 2484–2496
49. Castillo, R., Andres, J., and Moliner, V. (1999) Catalytic mechanism of dihydrofolate reductase enzyme. A combined quantum-mechanical molecular-mechanical characterization of transition state structure for the hydride transfer step. *J. Am. Chem. Soc.* **121,** 12140–12147
50. Ferrer, S., Silla, E., Tuñón, I., Martí, S., and Moliner, V. (2003) Catalytic mechanism of dihydrofolate reductase enzyme. A combined quantum-mechanical/molecular-mechanical characterization of the N5 protonation step. *J. Phys. Chem. B* **107,** 14036–14041
51. Brooks, B. R., Brooks, C. L., 3rd, Mackerell, A. D., Jr., Nilsson, L., Petrella, R. J., Roux, B., Won, Y., Archontis, G., Bartels, C., Boresch, S., Caflisch, A., Caves, L., Cui, Q., Dinner, A. R., Feig, M., *et al.* (2009) CHARMM: the biomolecular simulation program. *J. Comput. Chem.* **30,** 1545–1614

52. Brooks, B. R., Bruccoleri, R. E., Olafson, B. D., States, D. J., Swaminathan, S., and Karplus, M. (1983) CHARMM: a program for macromolecular energy, minimization, and dynamics calculations. *J. Comput. Chem.* **4,** 187–217
53. Warshel, A., and Levitt, M. (1976) Theoretical studies of enzymic reactions—dielectric, electrostatic and steric stabilization of carbonium-ion in reaction of lysozyme. *J. Mol. Biol.* **103,** 227–249
54. Dewar, M. J. S. (1985) Applications of quantum-mechanical molecular-models to chemical problems.70. Quantum-mechanical molecular-models. *J. Phys. Chem.* **89,** 2145–2150
55. Rossi, I., and Truhlar, D. G. (1995) Parameterization of NDDO wavefunctions using genetic algorithms. An evolutionary approach to parameterizing potential energy surfaces and direct dynamics calculations for organic reactions. *Chem. Phys. Lett.* **233,** 231–236
56. Jorgensen, W. L., Chandrasekhar, J., Madura, J. D., Impey, R. W., and Klein, M. L. (1983) Comparison of simple potential functions for simulating liquid water. *J. Chem. Phys.* **79,** 926–935
57. Best, R. B., Mittal, J., Feig, M., and MacKerell, A. D., Jr. (2012) Inclusion of many-body effects in the additive CHARMM protein CMAP potential results in enhanced cooperativity of α-helix and β-hairpin formation. *Biophys. J.* **103,** 1045–1051
58. Best, R. B., Zhu, X., Shim, J., Lopes, P. E., Mittal, J., Feig, M., and Mackerell, A. D., Jr. (2012) Optimization of the additive CHARMM all-atom protein force field targeting improved sampling of the backbone φ, ψ and side-chain χ_1 and χ_2 dihedral angles. *J. Chem. Theory Comput.* **8,** 3257–3273
59. Mackerell, A. D. (2004) Empirical force fields for biological macromolecules: overview and issues. *J. Comput. Chem.* **25,** 1584–1604
60. MacKerell, A. D., Bashford, D., Bellott, M., Dunbrack, R. L., Evanseck, J. D., Field, M. J., Fischer, S., Gao, J., Guo, H., Ha, S., Joseph-McCarthy, D., Kuchnir, L., Kuczera, K., Lau, F. T., Mattos, C., *et al.* (1998) All-atom empirical potential for molecular modeling and dynamics studies of proteins. *J. Phys. Chem. B* **102,** 3586–3616
61. Nam, K., Gao, J., and York, D. M. (2005) An efficient linear-scaling Ewald method for long-range electrostatic interactions in combined QM/MM calculations. *J. Chem. Theory Comput.* **1,** 2–13
62. Andersen, H. C. (1980) Molecular dynamics simulations at constant pressure and/or temperature. *J. Chem. Phys.* **72,** 2384–2393
63. Feller, S. E., Zhang, Y., Pastor, R. W., and Brooks, B. R. (1995) Constant pressure molecular dynamics simulation: the Langevin piston method. *J. Chem. Phys.* **103,** 4613–4621
64. Hoover, W. G. (1985) Canonical dynamics: equilibrium phase-space distributions. *Phys. Rev. A* **31,** 1695–1697
65. Hockney, R. W. (1970) The potential calculation and some applications. *Methods Comput. Phys.* **9,** 135–211
66. Ryckaert, J.-P., Ciccotti, G., and Berendsen, H. J. (1977) Numerical integration of the Cartesian equations of motion of a system with constraints: molecular dynamics of n-alkanes. *J. Comput. Phys.* **23,** 327–341
67. Torrie, G. M., and Valleau, J. P. (1977) Nonphysical sampling distributions in Monte Carlo free-energy estimation: umbrella sampling. *J. Comput. Phys.* **23,** 187–199
68. Kumar, S., Rosenberg, J. M., Bouzida, D., Swendsen, R. H., and Kollman, P. A. (1992) The weighted histogram analysis method for free-energy calculations on biomolecules. I. The method. *J. Comput. Chem.* **13,** 1011–1021
69. Hub, J. S., de Groot, B. L., and van der Spoel, D. (2010) g_wham—a free weighted histogram analysis implementation including robust error and autocorrelation estimates. *J. Chem. Theory Comput.* **6,** 3713–3720
70. Gao, J. (1992) Absolute free energy of solvation from Monte Carlo simulations using combined quantum and molecular mechanical potentials. *J. Phys. Chem.* **96,** 537–540
71. Li, G., and Cui, Q. (2003) pK_a calculations with QM/MM free energy perturbations. *J. Phys. Chem. B* **107,** 14521–14528
72. Warshel, A., Sussman, F., and King, G. (1986) Free energy of charges in solvated proteins: microscopic calculations using a reversible charging process. *Biochemistry* **25,** 8368–8372
73. Maharaj, G., Selinsky, B. S., Appleman, J. R., Perlman, M., London, R. E., and Blakley, R. L. (1990) Dissociation constants for dihydrofolic acid and dihydrobiopterin and implications for mechanistic models for dihydrofolate reductase. *Biochemistry* **29,** 4554–4560